Progress In Electromagnetics Research, Vol. 143, 675–708, 2013

MICROWAVE IMAGING WITHIN THE INTERVAL ANALYSIS FRAMEWORK

Paolo Rocca, Matteo Carlin, Luca Manica, and Andrea Massa*

ELEDIA Research Center, Department of Information Engineering and Computer Science, University of Trento, Via Sommarive 5, Trento 38123, Italy

Abstract—An approach based on the use of the arithmetic of intervals and Interval Analysis for the solution of inverse scattering problems is presented and assessed. By exploiting the property of the Interval Analysis to find the global minimum of a functional in a n-dimensional space, the proposed approach adopts a branch and bound process to discard the regions of the solutions space not containing the global solution, while keeping those where a feasible solution is expected until a suitable converge criterion is reached. A representative set of results concerned with the reconstruction of circular dielectric objects within the first-order Born approximation are reported and discussed to show potentialities and current limitations of the proposed approach.

1. INTRODUCTION

The goal of electromagnetic inverse scattering [1, 2] is the retrieval of the physical parameters (i.e., the dielectric permittivity and the electric conductivity in case of non-magnetic targets as those considered in this contribution) and/or the geometrical features of unknown scatterers embedded in an inaccessible domain and probed by a set of known microwave radiations. The data, namely the scattered field derived from the interactions between the incident radiations and the objects, are measured on a set of sensors, placed outside the area under test, in the so-called observation domain. Although the problem has been widely studied in the last decades and non-negligible advances have been yielded in terms of efficiency, robustness, and efficacy of the inversion methods, the interest and the need of defining more and more effective solvers still remains as confirmed by the number of

Received 3 August 2013, Accepted 29 October 2013, Scheduled 11 December 2013

* Corresponding author: Andrea Massa (andrea.massa@unitn.it).

journal articles published every year on this subject (see [3–55] and the references cited therein for an overview) and the sessions worldwide organized in annual conference meetings. This is indicative of the attention on this subject from academic, industrial, and governmental researchers and experts. As a matter of fact, the range of potential applications is wide and it spans from the more traditional (e.g., geophysical investigations and remote sensing [3–5], nondestructive testing and evaluation [6–10], and medical imaging [11–18]) to the latest ones mainly related to security and surveillance (e.g., through-the-wall imaging [19–24]) up to more recent applications [25].

It is well known that inverse scattering problems are affected by ill-posedness and non-linearity due to the finite amount of "information" available in the scattered field data [26, 27]. In order to avoid non-uniqueness and instability as well as to prevent the retrieval of false solutions [28], several inversion strategies have been proposed based on (*a*) a suitable definition of the integral equations either in exact [29, 30] or approximated [31–35] forms to model the scattering phenomena, (*b*) the exploitation of the available *a-priori* information on some features of the scenario/scatterers under test [15, 36–39] or/and the knowledge of input-output samples of data and reference solutions [40–42] and/or the information acquired during the inversion process [43–47], and (*c*) the use of suitable global optimization strategies [48–55]. Whatever the approach, inversion methods generally consider an optimization step aimed at minimizing/maximizing a suitably defined data-mismatch cost function through gradient or evolutionary-based algorithms with still not fully resolved drawbacks. On the one hand, the use of local optimizers (e.g., gradient based) requires the optimization process starts in the "attraction basin" [54] of the global optimum to avoid being trapped into local minima (i.e., false solutions) of the cost function. On the other hand, global optimizers do not guarantee the retrieval of the global optimum within a finite amount of time/iterations. Moreover, there is no evidence that the retrieved solution is the global one since the stopping criteria, generally based on the stationarity of the cost function or a maximum number of iterations, do not allow an exhaustive sampling of the solution space.

The approach proposed in this paper is aimed at addressing such a topic and it is based on the exploitation of the *Interval Analysis* (*IA*) and the *Interval Arithmetic*. Originally introduced to bound rounding errors in numeric computations [56, 57], the use of interval analysis has been then extended to the solution of linear and non-linear equations [58] and functional optimization [67]. Nowadays, the use of interval analysis is widespread, but its applications to electromagnetics are still limited to few applications mainly concerned

with the design of robust devices [59, 60] and reliable systems [61]. In this work, the reliability of the IA in the global optimum search as well as the intrinsic convergence conditions are exploited to define an innovative optimization framework where the inversion problem is firstly reformulated within the intervals arithmetic to successively apply an IA-based optimization for identifying the global optimum of the cost function at hand. A set of numerical experiments considering weak scattering conditions is reported and discussed to show the effectiveness of the approach in attaining the global optimum solutions.

The outline of the paper is as follows. The problem is mathematically formulated according to the principles of the arithmetic of intervals in Section 2, while Section 3 is devoted to present the IA-based optimization strategy. Numerical inversions of dielectric scatterers within the first-order Born approximation are then reported (Section 4) to illustrate the behavior of the approach (Section 4.1), to assess its robustness against noisy data (Section 4.2), and to evaluate its effectiveness in reconstructing targets different in dimensions and contrasts (Section 4.3). Eventually, some concluding remarks are drawn in Section 5, where the innovative features and the peculiarities of the proposed approach are pointed out also to envisage possible future extensions and improvements.

2. MATHEMATICAL FORMULATION

Let us consider a two-dimensional ($2D$) microwave imaging setup where a cylindrical object belongs to an inaccessible investigation domain Γ_{inv} probed by a set of V incident TM-polarized electromagnetic plane waves, $\underline{E}^v_{inc}(x,y,z) = E^v_{inc}(x,y)\,\underline{\hat{z}},\ v = 1,\ldots,V$ characterized by an angular frequency ω. The dielectric properties of the material in Γ_{inv} are unknown and modelled by means of the object function τ

$$\tau(x,y) = \begin{cases} \epsilon_r(x,y) - 1 - j\frac{\sigma(x,y)}{\omega\epsilon_0} & (x,y) \in \Omega \\ 0 & (x,y) \notin \Omega \end{cases} \tag{1}$$

Ω is the support of the scatterer where $\tau(x,y) \neq 0$, ϵ_r the dielectric permittivity, and σ the electric conductivity. A lossless non-magnetic background is assumed with a dielectric permittivity equal to ϵ_0. The relationships between the object and the scattered field $E^v_{scatt}(x,y)$, $v = 1,\ldots,V$ are mathematically described through the Lippman-Schwinger integral equation [1]

$$E^v_{scatt}(x_m,y_m) = \int_{\Gamma_{inv}} \tau(x',y')E^v_{tot}(x',y')G^v_{2D}(x,y\,|x',y')dx'dy' \qquad m = 1,\ldots,M;\ \ v = 1,\ldots,V \tag{2}$$

where $E^v_{scatt}(x_m, y_m) \triangleq E^v_{tot}(x_m, y_m) - E^v_{inc}(x_m, y_m)$, (x_m, y_m), $m = 1, \ldots, M$, being a set of sensor locations in the observation domain Γ_{obs}, external to Γ_{inv}, where the field data are collected. In (2), $E^v_{tot}(x, y)$, $v = 1, \ldots, V$ is the total field (i.e., the field measured when the target is present in Γ_{inv}) and $G^v_{2D}(x, y\,|x', y')$ is the $2D$ Green's function of the background medium [62]. In case of weak scatterers, the first-order Born approximation [63] holds true and the total field within the investigation domain can be approximated as $E^v_{tot}(x, y) = E^v_{inc}(x, y)$, $(x, y) \in \Gamma_{inv}$. Since the incident field (i.e., the field without the object) in Γ_{inv} can be measured during the calibration of the imaging system or it can be estimated, the source of the probing field being known, Equation (2) turns out to be linear with respect to the unknown object function τ.

In order to retrieve the τ distribution within the investigation domain, Equation (2) is firstly discretized. Towards this end, Γ_{inv} is partitioned into N sub-domains, Γ_n, $n = 1, \ldots, N$, where both the object function (1) and the incident field values are assumed to be piecewise constant

$$\begin{aligned} \tau(x, y) &= \sum_{n=1}^{N} \tau_n B_n(x, y) \\ E^v_{inc}(x, y) &= \sum_{n=1}^{N} E^v_{inc,n} B_n(x, y) \end{aligned} \tag{3}$$

$B_n(x, y)$ being a rectangular pulse basis function. Because of the presence of an unavoidable noise on the measured data samples collected in Γ_{obs}, a generalized solution has to be looked for [1] by minimizing the following cost function [64]

$$\Phi(\underline{\tau}) = \frac{\displaystyle\sum_{v=1}^{V}\sum_{m=1}^{M} \left\| E^v_{scatt,m} - \sum_{n=1}^{N} \tau_n E^v_{inc,n} G^v_{m,n} \right\|^2}{\displaystyle\sum_{v=1}^{V}\sum_{m=1}^{M} \left\| E^v_{scatt,m} \right\|^2} \tag{4}$$

where $\underline{\tau} = \{\tau_n,\, n = 1, \ldots, N\}$, $E^v_{scatt,m}$ is the scattered field measured at $(x_m,\, y_m)$, $G^v_{m,n} = \int_{\Gamma_n} G^v_{2D}(x_m,\, y_m | x', y')\, dx' dy'$, $\|\,.\,\|$ being the L^2 norm.

Unlike standard approaches, the goal of the IA when applied to inverse scattering problems is not the retrieval of the object function $\underline{\tau}$, but the definition of the interval vector $[\underline{\tau}] = \{[\tau_n],\, n = 1, \ldots, N\}$ (see Appendix A) to which the actual solution belongs to (i.e., $\underline{\tau}^{act} \in [\tau]$):

the smaller the interval, the lower/greater is the uncertainty/precision in determining the final solution. With reference to (3), it means that a set of solutions/objects, more precisely an *interval of solutions*, is taken into account

$$[\tau(x,y)] = \sum_{n=1}^{N} [\tau_n] B_n(x,y) \tag{5}$$

where $[\tau(x,y)]$ is an interval of contrast distributions. By substituting (5) in (2) and performing the mathematical operations according to the arithmetic of intervals (see Appendix B) and the Fundamental Theorem of IA (see Appendix C), the IA counterpart, $[\Phi([\underline{\tau}])]$, of the cost function in (4) assumes the following explicit expression

$$[\Phi([\underline{\tau}])] = \frac{\sum_{v=1}^{V}\sum_{m=1}^{M}\left\| E^v_{scatt,m} - \sum_{n=1}^{N}[\tau_n] E^v_{inc,n} G^v_{m,n} \right\|^2}{\sum_{v=1}^{V}\sum_{m=1}^{M}\left\| E^v_{scatt,m} \right\|^2}. \tag{6}$$

3. IA-based OPTIMIZATION

In order to determine the optimal interval $[\underline{\tau}]^{opt}$ containing the actual contrast [i.e., the global optimum of the cost function in (4)], $\underline{\tau}^{act} \in [\tau]^{opt}$, the minimization of (6) is carried out by applying the "branch

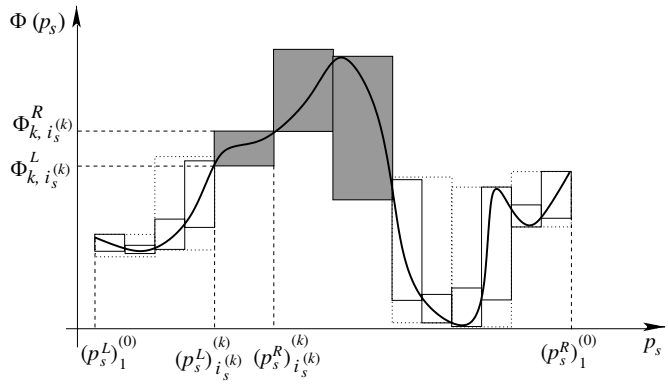

Figure 1. IA-based approach — Intervals and sketch of the branch-and-bound for functional optimization.

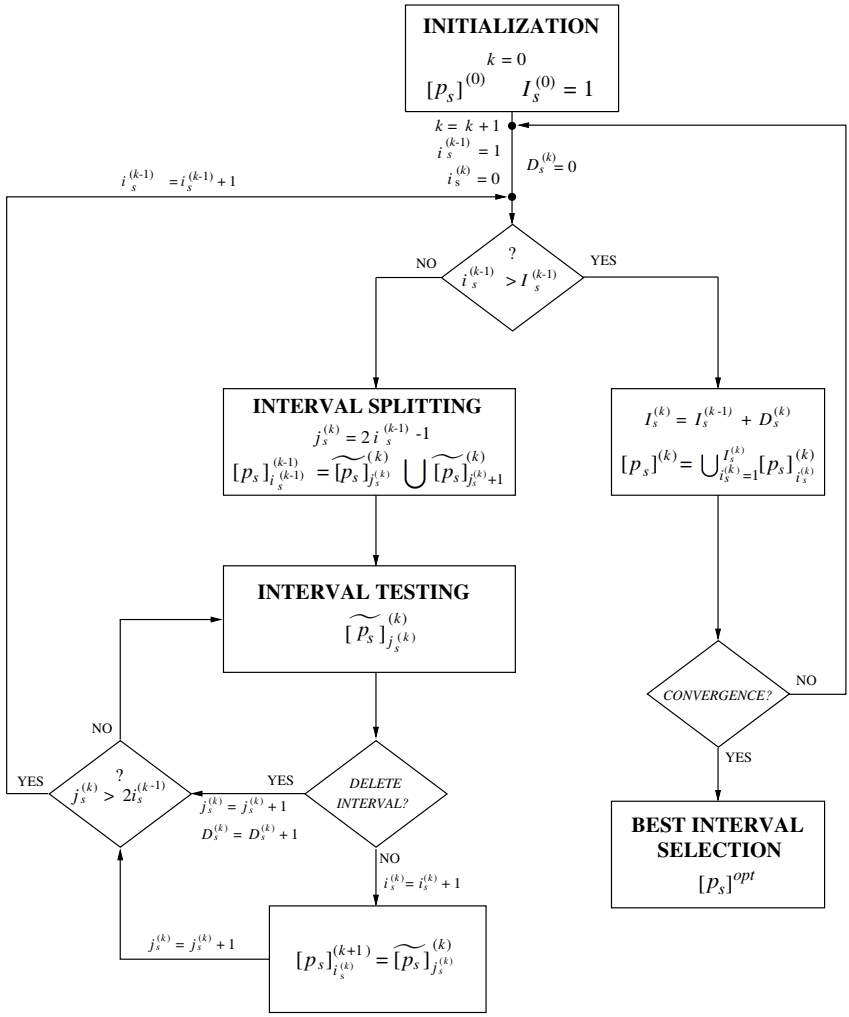

Figure 2. IA-based approach — Flowchart of the interval splitting and testing IA-based procedure.

and bound" technique (BB) as pictorially summarized in Fig. 1. With reference to a model-based representation of the scatterer in terms of a set of S descriptors†, $[\underline{P}] = \{[p_s] = [p_s^L, p_s^R]: \ s = 1, \ldots, S\}$, the BB iteratively splits the initial interval $[\underline{P}]^{(k)}$, $k = 0$ (k being the

† Please notice that the case $S = N$ reduces to the pixel-representation of the scatterer, while in general it can "code" either qualitative/geometrical (i.e., shape, position) and/or quantitative (i.e., dielectric values) scatterer descriptors.

iteration index), which extends to the whole solution space, into sub-intervals discarding those (e.g., black-boxes in Fig. 1) not containing the global minimum $\underline{P}^{opt}$ until the convergence ($k = K$). The process works as shown in Fig. 2 where, for the sake of description simplicity, only a single descriptor (i.e., the s-th parameter p_s) has been taken into account being the extension to the multi-parameter case, although mathematically straightforward, quite complex to be pictorially described. More specifically,

- **Step 0** — *Initialization* ($k = 0$). Set the bounds of the initial single interval of the s-th parameter ($I_s^{(k)} = 1$) such as $[p_s]^{(k)} = [p_s]_{i_s^{(k)}=1}^{(k)} = [p_s^L, p_s^R]$, $i_s^{(k)}$ and $I_s^{(k)}$ being the interval index ($i_s^{(k)} = 1, \ldots, I_s^{(k)}$) and the total number of intervals of the s-th descriptor at the k-th iteration, respectively. Update the iteration index, $k \leftarrow k + 1$, and go to Step 1;
- **Step 1** — *IA-based Optimization Loop*. Set $i_s^{(k-1)} = 1$, $i_s^{(k)} = 0$, and $D_s^{(k)} = 0$, $D_s^{(k)}$ being the number of intervals of the s-th descriptor deleted at the k-th iteration. Perform the following steps:
  - **Step 1.a** — *Interval Splitting*. Split the interval $[p_s]_{i_s^{(k-1)}}^{(k-1)}$ into two sub-intervals, $\widetilde{[p_s]}_{j_s^{(k)}}^{(k)}$ and $\widetilde{[p_s]}_{j_s^{(k)}+1}^{(k)}$ as shown in Fig. 3 and defined as
$$\begin{aligned} \widetilde{[p_s]}_{j_s^{(k)}}^{(k)} &= [p_s^L, \chi]_{i_s^{(k-1)}}^{(k-1)} \\ \widetilde{[p_s]}_{j_s^{(k)}+1}^{(k)} &= [\chi, p_s^R]_{i_s^{(k-1)}}^{(k-1)} \end{aligned} \tag{7}$$
    where $\chi = m[p_s]_{i_s^{(k-1)}}^{(k-1)}$ is the mid point of the interval $[p_s]_{i_s^{(k-1)}}^{(k-1)}$ and $j_s^{(k)} = 2 \times i_s^{(k-1)} - 1$. Therefore, it turns out that $[p_s]_{i_s^{(k-1)}}^{(k-1)} = \widetilde{[p_s]}_{j_s^{(k)}}^{(k)} \cup \widetilde{[p_s]}_{j_s^{(k)}+1}^{(k)}$;
  - **Step 1.b** — *Interval Testing*. Check if the two sub-intervals in (7) could potentially contain the global optimum (i.e., minimum) according to the so-called "*lower-bound*" test. Let $\widetilde{\Phi}_{k,j_s^{(k)}}^L$ ($\Phi_{k-1,i_s^{(k-1)}}^L$) and $\widetilde{\Phi}_{k,j_s^{(k)}}^R$ ($\Phi_{k-1,i_s^{(k-1)}}^R$) be the left and the right endpoints of the interval function $[\Phi]$ within the interval $\widetilde{[\underline{P}]}_{j_s^{(k)}}^{(k)}$ ($[\underline{P}]_{i_s^{(k-1)}}^{(k-1)}$), namely $[\Phi(\widetilde{[\underline{P}]}_{j_s^{(k)}}^{(k)})] = [\widetilde{\Phi}_{k,j_s^{(k)}}^L, \widetilde{\Phi}_{k,j_s^{(k)}}^R]$ ($[\Phi([\underline{P}]_{i_s^{(k-1)}}^{(k-1)})] = [\Phi_{k-1,i_s^{(k-1)}}^L, \Phi_{k-1,i_s^{(k-1)}}^R]$), if

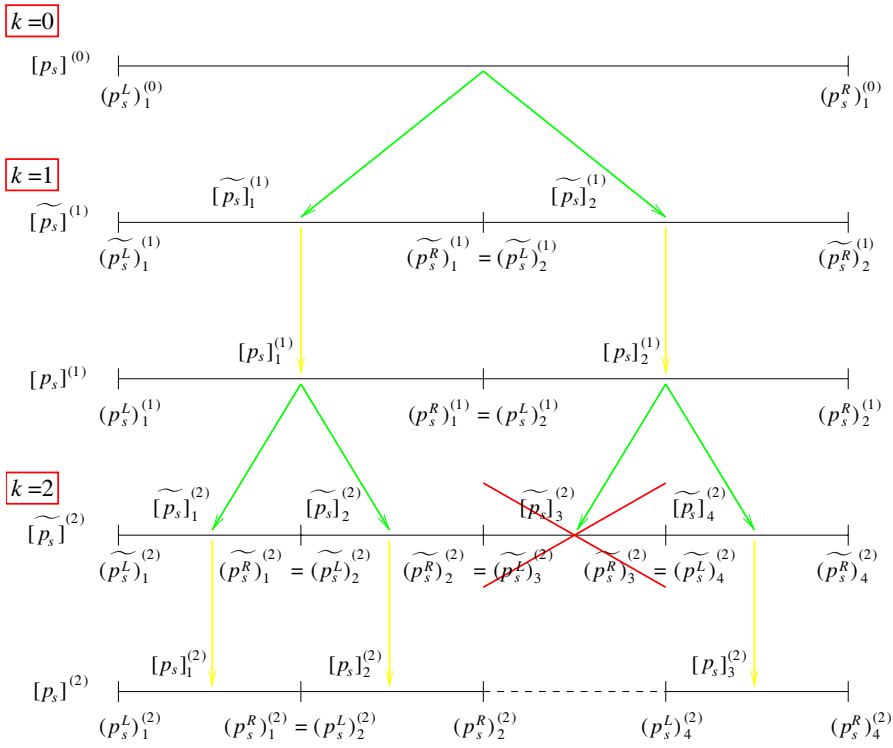

Figure 3. IA-based approach — Splitting and testing of intervals according to the procedure of Fig. 2.

$\widetilde{\Phi}^{L}_{k,j_s^{(k)}} > \widetilde{\Phi}^{R}_{k,\iota_s^{(k)}}$ or $\widetilde{\Phi}^{L}_{k,j_s^{(k)}} > \Phi^{R}_{k-1,\iota_s^{(k-1)}}$, $\iota_s^{(k)} = 1,\ldots,j_s^{(k)}+1$, $\iota_s^{(k)} \neq j_s^{(k)}$, $\iota_s^{(k-1)} = i_s^{(k-1)}+1,\ldots,I_s^{(k-1)}$, then discard the interval vector $\widetilde{[\underline{P}]}^{(k)}_{j_s^{(k)}} = (\widetilde{[p_s]}^{(k)}_{j_s^{(k)}};\ s = 1,\ldots,S)$ and update $D_s^{(k)}$ ($D_s^{(k)} = D_s^{(k)}+1$). The same evaluation is done for interval $\widetilde{[\underline{P}]}^{(k)}_{j_s^{(k)}+1}$. Doing so, one of the following event verifies:

- **Interval Deletion** — Both sub-intervals are deleted, namely $\widetilde{[p_s]}^{(k)}_{j_s^{(k)}} \Rightarrow \emptyset$ and $\widetilde{[p_s]}^{(k)}_{j_s^{(k)}+1} \Rightarrow \emptyset$, then $[p_s]^{(k-1)}_{i_s^{(k-1)}} \Rightarrow \emptyset$ and $D_s^{(k)} = D_s^{(k)}+2$;
- **Interval Preservation** — Both $\widetilde{[p_s]}^{(k)}_{j_s^{(k)}}$ and $\widetilde{[p_s]}^{(k)}_{j_s^{(k)}+1}$ (i.e., $[p_s]^{(k)}_{i_s^{(k)}+1} = \widetilde{[p_s]}^{(k)}_{j_s^{(k)}}$ and $[p_s]^{(k)}_{i_s^{(k)}+2} = \widetilde{[p_s]}^{(k)}_{j_s^{(k)}+1}$) are

kept then $[p_s]^{(k-1)}_{i_s^{(k-1)}} \Rightarrow \widetilde{[p_s]}^{(k)}_{j_s^{(k)}} \cup \widetilde{[p_s]}^{(k)}_{j_s^{(k)}+1}$ and $i_k \leftarrow i_k + 2$;

∗ **Interval Reduction** — Only half interval is maintained (i.e., $[p_s]^{(k)}_{i_s^{(k)}+1} = \widetilde{[p_s]}^{(k)}_{j_s^{(k)}}$ if $\widetilde{[p_s]}^{(k)}_{j_s^{(k)}+1} \Rightarrow \emptyset$ or $[p_s]^{(k)}_{i_s^{(k)}+1} = \widetilde{[p_s]}^{(k)}_{j_s^{(k)}+1}$ if $\widetilde{[p_s]}^{(k)}_{j_s^{(k)}} \Rightarrow \emptyset$) then $[p_s]^{(k-1)}_{i_s^{(k-1)}} \Rightarrow \begin{cases} \widetilde{[p_s]}^{(k)}_{j_s^{(k)}} & if\ \widetilde{[p_s]}^{(k)}_{j_s^{(k)}+1} \Rightarrow \emptyset \\ \widetilde{[p_s]}^{(k)}_{j_s^{(k)}+1} & if\ \widetilde{[p_s]}^{(k)}_{j_s^{(k)}} \Rightarrow \emptyset \end{cases}$, $i_k \leftarrow i_k + 1$, and $D_s^{(k)} = D_s^{(k)} + 1$;

Update the interval index ($i_s^{(k-1)} \leftarrow i_s^{(k-1)}+1$) and go Step 1.c;

– **Step 1.c** — *Iteration Termination Check* — If $i_s^{(k-1)} \leq I_s^{(k-1)}$ then go to Step 1.a, otherwise set $I_s^{(k)} = I_s^{(k-1)} - D_s^{(k)}$ and go to Step 2;

• **Step 2** — *Convergence Check* — Compose the admissible solution space at the k-th iteration as the union of the interval not deleted yet, $[p_s]^{(k)} = \bigcup_{i_s^{(k)}=1}^{I_s^{(k)}} [p_s]^{(k)}_{i_s^{(k)}}$, $s = 1, \ldots, S$, being $[p_s]^{(k)}_{i_s^{(k)}} = \left[\left(p_s^L\right)^{(k)}_{i_s^{(k)}}, \left(p_s^R\right)^{(k)}_{i_s^{(k)}} \right]$. Stop the iterative process related to the s-th parameter setting $k = K$ when $\left| \left(p_s^R\right)^{(k)}_{i_s^{(k)}} - \left(p_s^L\right)^{(k)}_{i_s^{(k)}} \right| < \delta_s$, δ_s being a user-defined threshold on the minimum width for a sub-interval of the s-th descriptor. Since generally $I_s^{(K)} > 1$ (i.e., multiple intervals wherein Φ values close to the optimal one have been defined), the final estimate for the s-th descriptor is chosen belonging to the interval whose upper value is minimum among the $I_s^{(K)}$ remaining intervals

$$[p_s]^{opt} = \arg \left\{ \min_{i_s^{(k)} = 1, \ldots, I_s^{(K)}} \left(\Phi^R_{k, i_s^{(k)}} \right) \right\}, \tag{8}$$

and it is defined as $p_s^{opt} = m[p_s]^{opt}$. Otherwise (i.e., $|(p_s^R)^{(k)}_{i_s^{(k)}} - (p_s^L)^{(k)}_{i_s^{(k)}}| \geq \delta_s$), $k \leftarrow k + 1$ and go to Step 1.

4. NUMERICAL ASSESSMENT AND VALIDATION

The performance of the proposed IA-based approach and its behavior are examined in the following by reporting and discussing representative results from a set of numerical experiments. The

reference geometry is a square investigation domain of side $L = 2\lambda$ probed by $V = 7$ TM-polarized plane waves impinging from directions $\theta_v = \frac{2\pi(v-1)}{V}$, $v = 1, \ldots, V$. For each v-th view, the field data (both amplitudes and phases) have been collected at $M = 7$ locations equally-spaced on a circle of radius $R = 5\lambda$. From a numerical point of view, such scattering data have been synthetically generated and successively blurred with an additive Gaussian noise, η, with zero mean and standard deviation [69] given by

$$\mathrm{dev}\{\eta\} = \frac{\sum_{v=1}^{V}\sum_{m=1}^{M} |E^v_{scatt}(x_m, y_m)|^2}{2 \times SNR \times \{M \times V\}}, \tag{9}$$

SNR being the signal-to-noise ratio. Moreover, the investigation domain Γ_{inv} has been partitioned for the inversion in a grid of $N_{inv} = 32 \times 32$ cells [65].

4.1. Off-centered Homogeneous Circular Cylinder

The first example deals with a lossless circular cylinder with homogeneous contrast $\tau^{act}(x, y) = 0.1$ and radius $\rho^{act} = 0.25\lambda$, located at $(x_c^{act}, y_c^{act}) = (-0.5\lambda, -0.5\lambda)$ as shown in Fig. 4(a). The measured field data have been synthetically generated by applying the forward

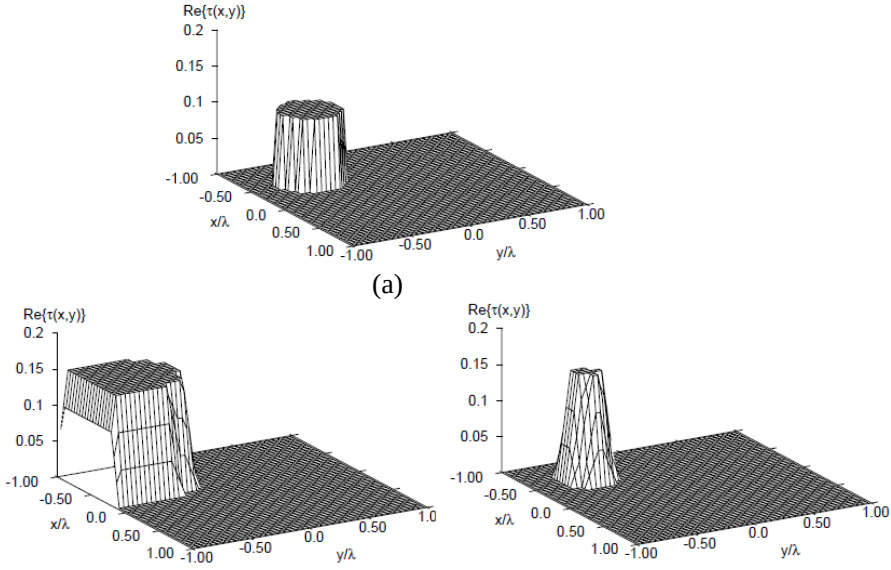

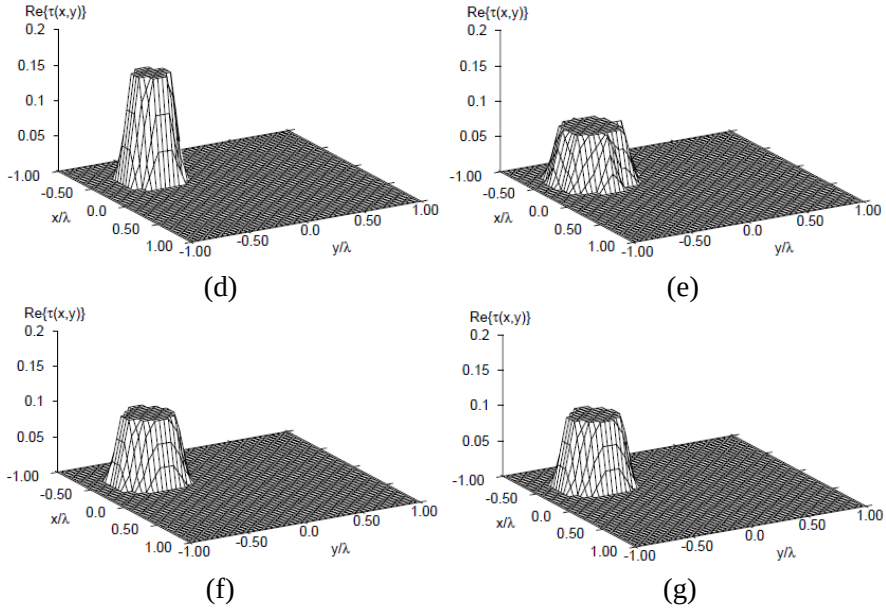

Figure 4. Off-centered homogeneous circular cylinder [$\rho = \frac{\lambda}{4}$, $\tau = 0.1$, $(x_c, y_c) = (-\frac{\lambda}{2}, -\frac{\lambda}{2})$, $SNR = 50\,\mathrm{dB}$]. Object Reconstruction — Distribution of the object function for (a) the actual solution and those retrieved by means of the IA-based approach when (b) $k = 1$, (c) $k = 3$, (d) $k = 5$, (e) $k = 7$, (f) $k = 9$, and (g) $k = K = 19$.

solver with a finer discretization grid ($N_{fwd} = 51 \times 51$) to avoid the "inverse crime" [66]. With reference to a model-based representation of the scatterer, the descriptors at hand are here the value of the object function τ and the geometrical parameters of the cylinder, namely the radius ρ and the center coordinates (x_c, y_c). Accordingly, the unknown interval vector turns out being of $S = 4$ descriptors: $[\underline{P}] = \{[p_s];\ s = 1, \ldots, S\} = \{[\tau], [\rho], [x_c], [y_c]\}$.

At the initialization of the IA-based inversion ($k = 0$), the intervals in Table 1 have been considered. The boundaries (i.e., minimum and maximum values) for each parameter have been selected, on the one hand, to encompass all the retrievable[‡] cylinders and, on the other, to avoid unfeasible solutions.

[‡] By virtue of the discretization of the inverse problem, the length of the side of each cell is $l = \frac{L}{\sqrt{N_{inv}}} = 0.0625\lambda$. Accordingly, the minimum radius of the object which can be mapped into the grid for the evaluation of the cost function (6), namely the left endpoint of $[\rho]^{(0)}$, has been set to $(\rho^L)_1^{(0)} = \frac{l}{2}$.

Table 1. Off-centered homogeneous circular cylinder [$\rho = \frac{\lambda}{4}$, $\tau = 0.1$, $(x_c, y_c) = (-\frac{\lambda}{2}, \frac{\lambda}{2})$, $SNR = 50\,\mathrm{dB}$]. *Initialization* — Intervals considered at the initialization $k = 0$ of the IA-based optimization process.

Unknown Parameter Intervals	*Feasible Solution Space*
$[\tau]^{(0)} = [(\tau^L)_1^{(0)}, (\tau^R)_1^{(0)}]$	$[0.0, 0.3]$
$[\rho]^{(0)} = [(\rho^L)_1^{(0)}, (\rho^R)_1^{(0)}]$	$[0.03125\lambda,\ 1.0\lambda]$
$[x_c]^{(0)} = [(x_c^L)_1^{(0)}, (x_c^R)_1^{(0)}]$	$[(-1.0 + (\rho^L)_1^{(0)})\lambda,$ $(1.0 - (\rho^L)_1^{(0)})\lambda]$
$[y_c]^{(0)} = [(y_c^L)_1^{(0)}, (y_c^R)_1^{(0)}]$	$[(-1.0 + (\rho^L)_1^{(0)})\lambda,$ $(1.0 - (\rho^L)_1^{(0)})\lambda]$

Figures 5 and 6 show the evolution of the *admissible* solutions space $\Omega^{(k)} = \bigcup_{i^{(k)}=1}^{I^{(k)}} [\underline{P}]_{i^{(k)}}^{(k)}$ throughout the optimization process where the colored regions belong to the union of the $I^{(k)}$ intervals that can potentially contain the optimal solution at the k-th iteration. Concerning the splitting and testing of the intervals, only the geometrical features (namely the coordinates of the center and the radius) have been considered at the beginning of the optimization process (until $|(p_s^R)_{i_s^{(k)}}^{(k)} - (p_s^L)_{i_s^{(k)}}^{(k)}| < \delta_s$, being $p_s = \{\rho,\ x_c,\ y_c\}$), while the contrast has been kept to the initial interval value (i.e., $[\tau]_{i^{(k)}}^{(k)} = [\tau]^{(0)}$). Such a choice has been adopted to point out the effectiveness of the approach when used as a qualitative inversion strategy and then as a quantitative reconstruction method.

At the end of the "qualitative" step ($k = 5 - \Lambda^{(k)} = \sum_{\xi=1}^{k} I^{(\xi)} = 17949$) when the maximum subdivision of the intervals for ρ and (x_c, y_c) has been obtained, the portion of the solution space still admissible, namely $\Omega_{\{x_c,y_c\}}^{(k)} = \{\bigcup_{i^{(k)}=1}^{I^{(k)}} [x_c]_{i^{(k)}}^{(k)}, \bigcup_{i^{(k)}=1}^{I^{(k)}} [y_c]_{i^{(k)}}^{(k)}\}$ and $\Omega_{\{x_c,y_c,\rho\}}^{(k)} = \{\bigcup_{i^{(k)}=1}^{I^{(k)}} [x_c]_{i^{(k)}}^{(k)}, \bigcup_{i^{(k)}=1}^{I_k} [y_c]_{i^{(k)}}^{(k)}, \bigcup_{i^{(k)}=1}^{I_k} [\rho]_{i^{(k)}}^{(k)}\}$, is shown in Figs. 5(e)–5(f) and it amounts to 25.17% and 74.57% (Table 2) of the whole solution space, respectively. As expected, the support of the scatterer is over-estimated because of the uncertainty on the value of the object function not defined yet. Successively ($k > 5$), the optimization of the dielectric properties takes place to also quantitatively image the scattering scenario a hand. Fig. 6 shows the progressive reduction of the admissible solution space $\Omega_{\{x_c,y_c,\rho,\tau\}}^{(k)}$ until the actual value of

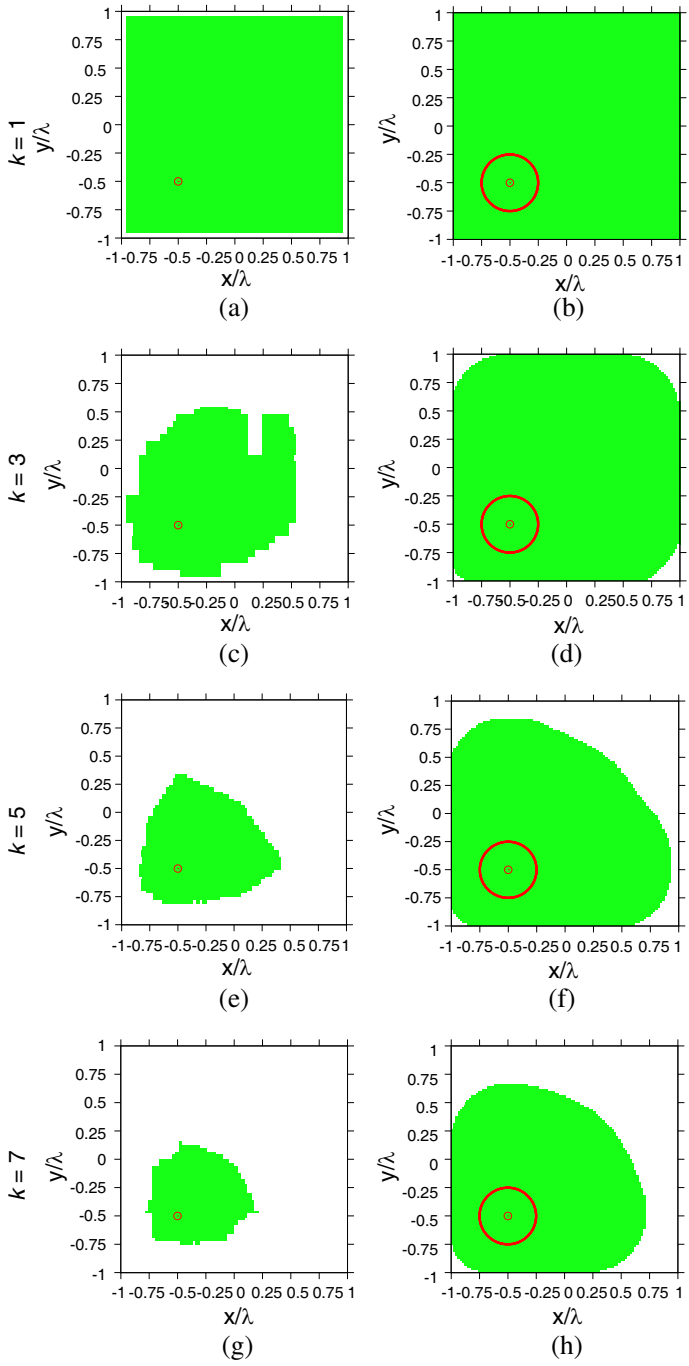
k = 1
k = 3
k = 5
k = 7
y/λ
x/λ
(a)
(b)
(c)
(d)
(e)
(f)
(g)
(h)

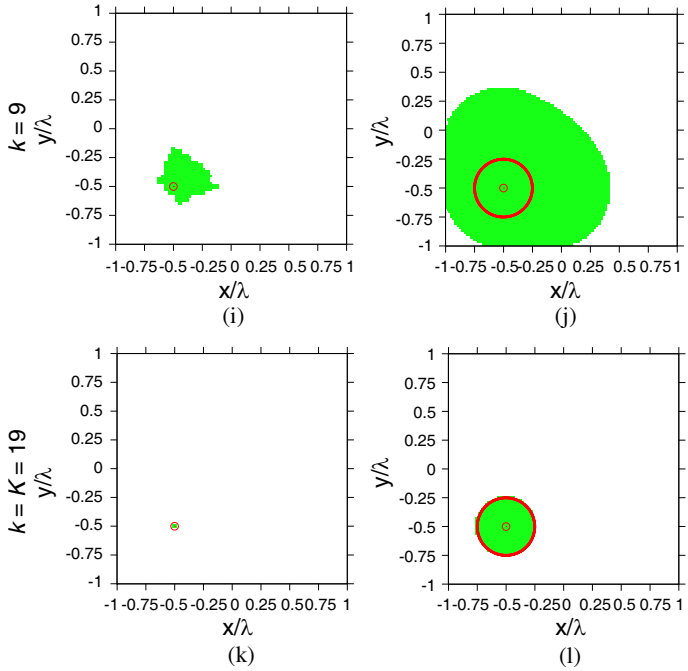

Figure 5. Off-centered homogeneous circular cylinder [$\rho = \frac{\lambda}{4}$, $\tau = 0.1$, $(x_c, y_c) = -\frac{\lambda}{2}, -\frac{\lambda}{2}$, $SNR = 50\,\text{dB}$]. IA-based Procedure Analysis — Admissible solution space when $k = \{1, 3, 5, 7, 9, K = 19\}$ related to (a), (c), (e), (g), (i), (k) the barycenter (i.e., $\Omega^{(k)}_{\{xc,yc\}}$) and (b), (d), (f), (h), (j), (l) the scatterer support $\Omega^{(k)}_{\{xc,yc,\rho\}}$).

the object function at convergence ($K = 19$) [Figs. 6(e)–6(f)] when $\Lambda^{(K)} = 51756$ different intervals have been evaluated. It is worth noting that, thanks to the optimization of the value of τ, not only the object function is correctly determined [Figs. 6(e) and 6(f)], but also the scatterer support turns out to be faithfully estimated as pointed out in Figs. 5(k)–5(l).

Figure 7 gives the number of admissible intervals $I^{(k)}$ versus the iteration number, k. As it can be observed, $I^{(k)}$ rapidly increases when only the qualitative reconstruction takes place because of the difficulty to delete intervals. Then, it drastically reduces when the also the scatterer contrast is processed. It is worth pointing out that the CPU-time in evaluating a single interval $T^{(k)}_{i^{(k)}}$ is almost constant

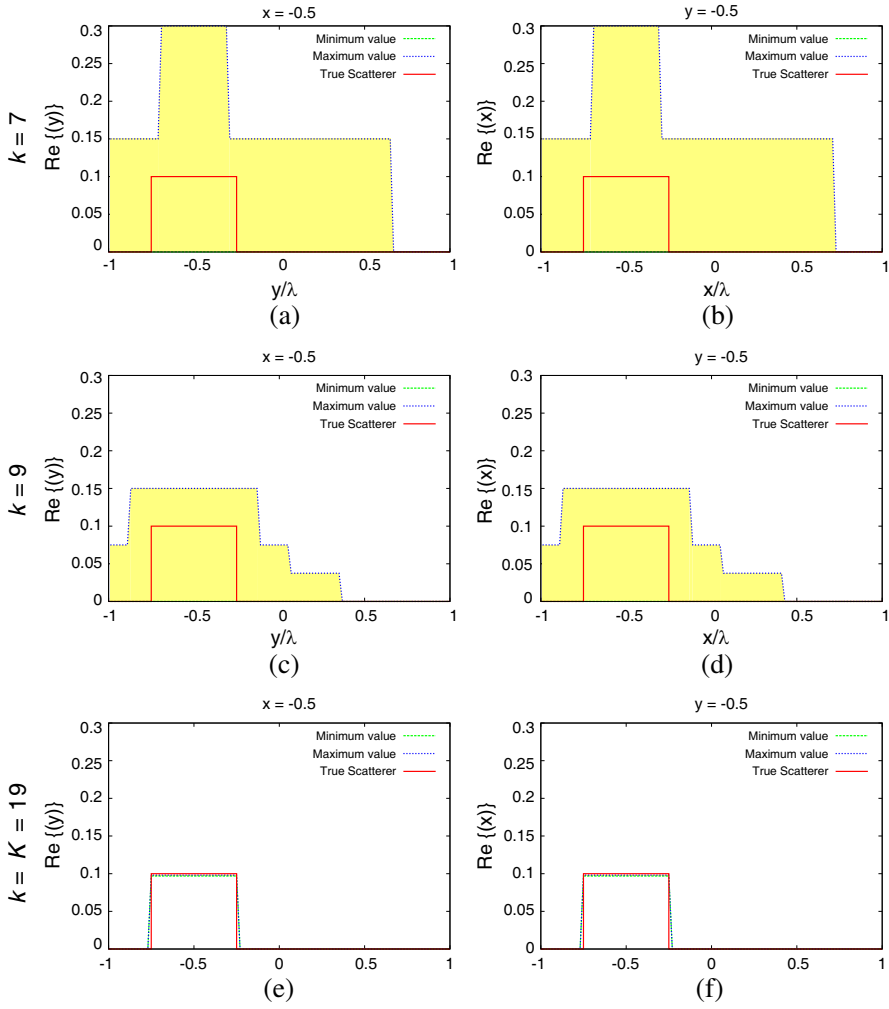

Figure 6. Off-centered homogeneous circular cylinder [$\rho = \frac{\lambda}{4}$, $\tau = 0.1$, $(x_c, y_c) = (-\frac{\lambda}{2}, -\frac{\lambda}{2})$, $SNR = 50\,\text{dB}$]. IA-based Procedure Analysis — Admissible solution space when $k = \{7, 9, K = 19\}$ related to the potential scatterers (i.e., $\Omega^{(k)}_{\{x_c, y_c, \rho, \tau\}}$): cuts of Γ_{inv} for (a), (c), (e) $x_c = 0.5\lambda$ and (b), (d), (f) $y_c = -0.5\lambda$.

and quite inexpensive[§] nevertheless the width of the interval. After $2.23 \times 10^3 [sec]$ (almost 0.6 hour), the dielectric profile generated from

[§] The simulations have been carried out on a 3 GHz PC with 2 GB of RAM.

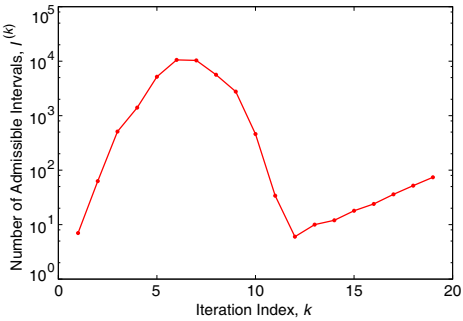

Figure 7. Off-centered homogeneous circular cylinder [$\rho = \frac{\lambda}{4}$, $\tau = 0.1$, $(x_c, y_c) = (-\frac{\lambda}{2}, -\frac{\lambda}{2})$, $SNR = 50$ dB]. IA-based Procedure Analysis — Number of "admissible" intervals at each iteration $I^{(k)}$, $k = 1, \ldots, K$.

Table 2. Off-centered homogeneous circular cylinder [$\rho = \frac{\lambda}{4}$, $\tau = 0.1$, $(x_c, y_c) = \left(-\frac{\lambda}{2}, -\frac{\lambda}{2}\right)$, $SNR = 50$ dB]. *IA-based Procedure Analysis* — Percentage of admissible solution space when $k = \{1, 3, 5, 7, 9, K = 19\}$ for the barycenter (i.e., $\Omega^{(k)}_{\{x_c,y_c\}}$) and the scatterer support $\Omega^{(k)}_{\{x_c,y_c,\rho\}}$).

k	1	3	5	7	9	19
$\Omega^{(k)}_{\{x_c,y_c\}}$ [%]	92.16	43.56	25.17	15.49	3.62	0.04
$\Omega^{(k)}_{\{x_c,y_c,\rho\}}$ [%]	100	96.33	74.57	60.65	39.99	5.42

the IA-optimized descriptors $\underline{P}^{opt} = \{x_c^{opt}, y_c^{opt}, \rho_c^{opt}, \tau_c^{opt}\}$ is that shown in Fig. 4(g). For completeness, the best reconstructions at the iterations in Table 2 are given in Fig. 4 whose corresponding intervals are reported in Table 3.

Concerning the quantitative evaluation of the reconstruction accuracy, the following error indexes have been computed

$$\xi_{reg} = \frac{1}{N_{reg}} \sum_{n=1}^{N_{reg}} \frac{\left|\tau^{act}(x_n, y_n) - \tau_n^{opt}\right|}{\left|\tau^{act}(x_n, y_n) + 1\right|} \tag{10}$$

τ^{act} and τ^{opt} being the relative dielectric permittivity of the actual object and the reconstructed one, respectively, while N_{reg} identifies either the number of discretization cells of the investigation domain ($reg \Rightarrow inv$, *total reconstruction error*) or the actual object support ($reg \Rightarrow int$, *internal reconstruction error*) or the background ($reg \Rightarrow$

Table 3. Off-centered homogeneous circular cylinder [$\rho = \frac{\lambda}{4}$, $\tau = 0.1$, $(x_c, y_c) = \left(-\frac{\lambda}{2}, -\frac{\lambda}{2}\right)$, $SNR = 50\,\text{dB}$]. *Object Reconstruction* — Intervals containing the best solutions retrieved by means of the IA-based approach when $k = \{1, 3, 5, 7, 9, K = 19\}$.

k	$[x_c]$	$[y_c]$
1	$[-0.726563, -0.484375]$	$[-0.968751, -0.484375]$
3	$[-0.605469, -0.484375]$	$[-0.605469, -0.484375]$
5	$[-0.514649, -0.484375]$	$[-0.514649, -0.484375]$
7	$[-0.514649, -0.484375]$	$[-0.514649, -0.484375]$
9	$[-0.514649, -0.484375]$	$[-0.514649, -0.484375]$
$K = 19$	$[-0.514649, -0.484375]$	$[-0.514649, -0.484375]$
k	$[\rho]$	$[\tau]$
1	$[0.031250, 0.273438]$	$[0.000000, 0.300001]$
3	$[0.031250, 0.091797]$	$[0.000000, 0.300001]$
5	$[0.152343, 0.182618]$	$[0.000000, 0.300001]$
7	$[0.243164, 0.273438]$	$[0.000000, 0.150001]$
9	$[0.212890, 0.243165]$	$[0.075000, 0.112501]$
$k = 19$	$[0.212890, 0.243165]$	$[0.097576, 0.097596]$

Table 4. Off-centered homogeneous circular cylinder [$\rho = \frac{\lambda}{4}$, $\tau = 0.1$, $(x_c, y_c) = (-\frac{\lambda}{2}, \frac{\lambda}{2})$, $SNR = 50\,\text{dB}$]. *Error Indexes* — Values of the error indexes of the best solutions retrieved by means of the IA-based approach when $k = \{1, 3, 5, 7, 9, k = 19\}$.

k	ξ_{inv}	ξ_{int}	ξ_{ext}	Δ_c	Δ_ρ
1	1.8×10^{-2}	4.6×10^{-2}	1.6×10^{-2}	1.6×10^{-1}	36.1
3	3.7×10^{-3}	7.3×10^{-2}	0.0	5.2×10^{-2}	38.7
5	3.1×10^{-3}	6.2×10^{-2}	0.0	0.0	29.5
7	2.5×10^{-3}	2.3×10^{-2}	1.4×10^{-3}	0.0	4.7
9	6.0×10^{-4}	7.0×10^{-3}	2.7×10^{-4}	0.0	14.7
$K = 19$	4.4×10^{-4}	3.6×10^{-3}	2.8×10^{-4}	0.0	14.7

ext, *external reconstruction error*). On the other hand, the qualitative imaging accuracy has been quantified in terms of the *location error*

$$\Delta_c = \frac{\sqrt{\left[x_c^{opt} - x_c^{act}\right]^2 + \left[y_c^{opt} - y_c^{act}\right]^2}}{\lambda} \tag{11}$$

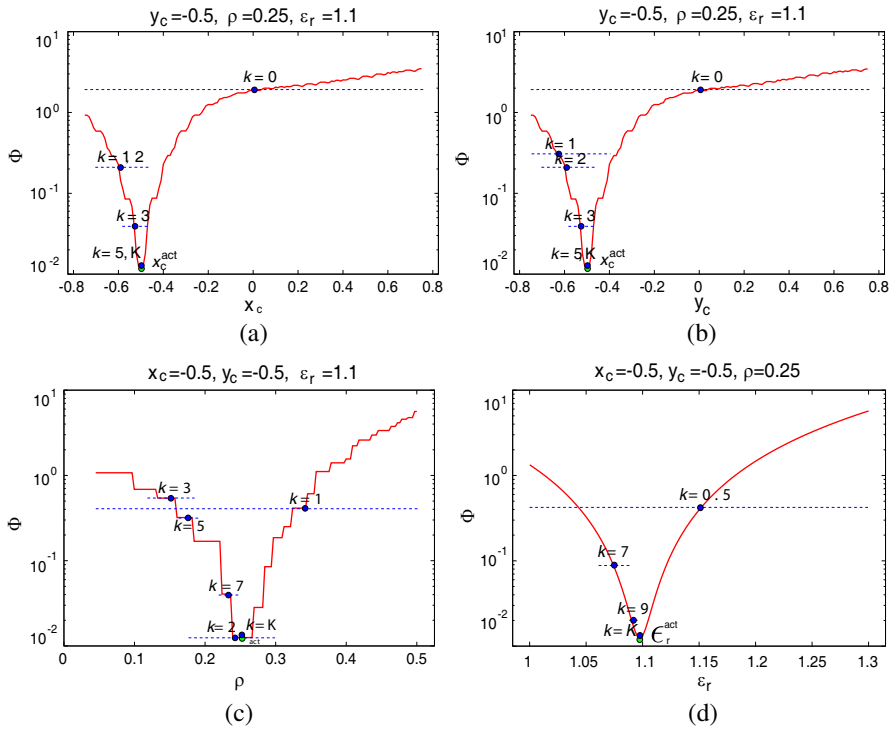

Figure 8. Off-centered homogeneous circular cylinder [$\rho = \frac{\lambda}{4}$, $\tau = 0.1$, $(x_c, y_c) = (-\frac{\lambda}{2}, -\frac{\lambda}{2})$, $SNR = 50\,\mathrm{dB}$]. Functional Analysis — Evolution of the parameter values $\{x_c^{(k)}, y_c^{(k)}, \rho^{(k)}, \tau^{(k)}\}$ estimated by means of the IA-based approach for the solutions in Fig. 4 and actual parameter values.

and the *occupation area error*

$$\Delta_\rho = \frac{\left|\rho^{opt} - \rho^{act}\right|}{\rho^{act}} \times 100, \tag{12}$$

(x_c, y_c) and ρ being the coordinates of the center and the equivalent radius of the object, respectively, and $x_c^{opt} = \frac{1}{2}\left(\frac{\sum_{n=1}^{N_{inv}}\left\{x_n \Re\left(\tau_n^{opt}\right)\right\}}{\sum_{n=1}^{N_{inv}}\left\{\Re\left(\tau_n^{opt}\right)\right\}} + \frac{\sum_{n=1}^{N_{inv}}\left\{x_n \Im\left(\tau_n^{opt}\right)\right\}}{\sum_{n=1}^{N_{inv}}\left\{\Im\left(\tau_n^{opt}\right)\right\}}\right)$, $y_c^{opt} = \frac{1}{2}\left(\frac{\sum_{n=1}^{N_{inv}}\left\{y_n \Re\left(\tau_n^{opt}\right)\right\}}{\sum_{n=1}^{N_{inv}}\left\{\Re\left(\tau_n^{opt}\right)\right\}} + \frac{\sum_{n=1}^{N_{inv}}\left\{y_n \Im\left(\tau_n^{opt}\right)\right\}}{\sum_{n=1}^{N_{inv}}\left\{\Im\left(\tau_n^{opt}\right)\right\}}\right)$, while $\rho^{opt} = \frac{1}{2}\left(\frac{\sum_{n=1}^{N_{inv}}\left\{\Re\left(\tau_n^{opt}\right)\frac{\sqrt{\left(x_n - x_c^{opt}\right)^2 - \left(y_n - y_c^{opt}\right)^2}}{\max_{n=1,\ldots,N_{inv}}\Re\left(\tau_n^{opt}\right)}\right\}}{\sum_{n=1}^{N_{inv}}\left\{\frac{\Re\left(\tau_n^{opt}\right)}{\max_{n=1,\ldots,N_{inv}}\Re\left(\tau_n^{opt}\right)}\right\}}\right)$

$$+\frac{\sum_{n=1}^{N_{inv}}\left\{\Im\left(\tau_n^{opt}\right)\frac{\sqrt{\left(x_n-x_c^{opt}\right)^2-\left(y_n-y_c^{opt}\right)^2}}{\max_{n=1,\ldots,N_{inv}}\Im\left(\tau_n^{opt}\right)}\right\}}{\sum_{n=1}^{N_{inv}}\left\{\frac{\Im\left(\tau_n^{opt}\right)}{\max_{n=1,\ldots,N_{inv}}\Im\left(\tau_n^{opt}\right)}\right\}}\Bigg), \Re(\,.\,) \text{ and } \Im(\,.\,) \text{ being the real}$$

and imaginary parts.

As for the test case under analysis, the value of the internal error, $\xi_{int}^K = 4.4 \times 10^{-4}$ (Table 4), confirms the effectiveness of the inversion with the reconstruction of the background without any artifacts ($\xi_{ext}^K = 2.8 \times 10^{-4}$ — Table 4).

In order to assess the reliability of the IA-approach in reaching the global optimum, a functional analysis has been carried whose results are summarized in Fig. 8 where, in each plot, the behavior of the functional (4) is reported by varying only one parameter within the range of values admitting physical solutions while the others are kept fixed to the actual parameter values $\{\tau^{act}, \rho^{act}, x_c^{act}, y_c^{act}\}$. Each sample of a graph gives the value of the estimated parameters for the solutions of Fig. 4. The dashed lines are related to the width of the corresponding solution intervals at the iteration indicated by the sample. As expected, the global optimum of the functional (i.e., the actual solution) is reached by the IA-based optimization strategy with an excellent precision since the interval width at $k = K$ is negligible and therefore representative of a uniform solution.

Finally, Fig. 9 shows the behavior of the quantitative errors for the best solution determined after the evaluation of each interval with the

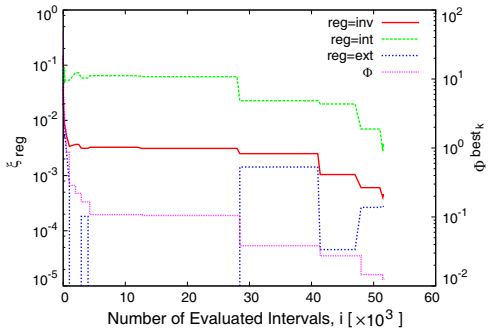

Figure 9. Off-centered homogeneous circular cylinder [$\rho = \frac{\lambda}{4}$, $\tau = 0.1$, $(x_c, y_c) = (-\frac{\lambda}{2}, -\frac{\lambda}{2})$, $SNR = 50\,\text{dB}$]. Error Indexes and Fitness Function — Values of the total, internal, and external error indexes and of the fitness function of the best solution retrieved through the IA-based optimization process after the evaluation of each interval.

corresponding values of the cost function. Both the total error and the cost function value monotonically decrease confirming the efficiency of the IA approach to step-by-step approximate the actual profile.

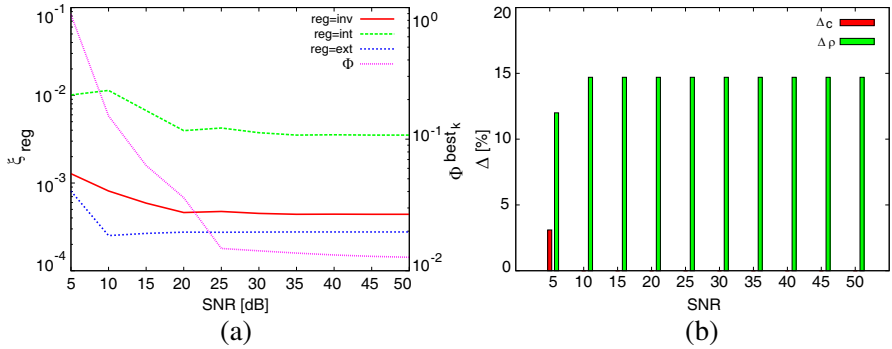

Figure 10. Off-centered homogeneous circular cylinder [$\rho = \frac{\lambda}{4}$, $\tau = 0.1$, $(x_c, y_c) = (-\frac{\lambda}{2}, -\frac{\lambda}{2})$, $SNR \in [5, 50]$ dB]. Error Indexes and Fitness Function — Plot of (a) the total, internal, and external error indexes and the fitness function and of (b) the location and occupation area error of the best solutions retrieved by means of the IA-based approach for different level of SNR.

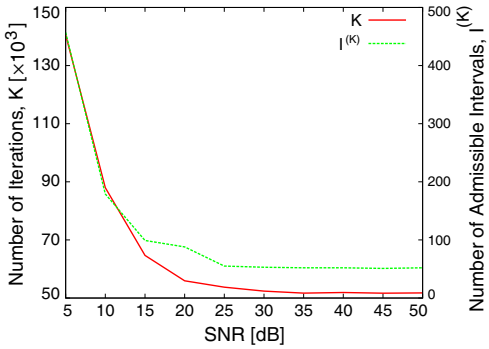

Figure 11. Off-centered homogeneous circular cylinder [$\rho = \frac{\lambda}{4}$, $\tau = 0.1$, $(x_c, y_c) = (-\frac{\lambda}{2}, -\frac{\lambda}{2})$, $SNR \in [5, 50]$ dB]. IA-based Procedure Analysis - Number of iterations required to determine the final solution and number of admissible intervals at convergence for different level of SNR.

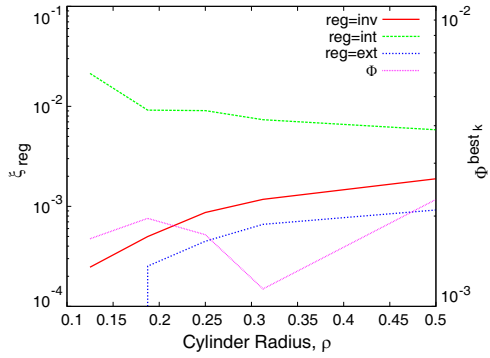

Figure 12. Off-centered homogeneous circular cylinder [$\rho \in [\frac{\lambda}{8}, \frac{\lambda}{2}]$, $\tau = 0.1$, $(x_c, y_c) = (\frac{\lambda}{4}, \frac{\lambda}{8})$, $SNR = 50\,\text{dB}$]. Error Indexes and Fitness Function — Values of the total, internal, and external error indexes and of the fitness function of the best solutions retrieved by means of the IA-based approach for different sizes of the actual object: $\rho = \{\frac{\lambda}{8}, \frac{\lambda}{5}, \frac{\lambda}{4}, \frac{\lambda}{3}, \frac{\lambda}{2}\}$

.

4.2. Robustness Analysis against Noise

To investigate on the robustness of the IA-based inversion to noisy data, the reconstruction of the same scatterer profile of the previous example has been performed by varying the noise level within the range $SNR = [5, 50]\,[\text{dB}]$. As indicated by the amount of the error indexes in Fig. 10, the scatterer retrieval turns out to be very accurate whatever the data blurring. As a matter of fact, the maximum total error results of about $\xi_{inv}^{K} = 10^{-3}$ when $SNR = 5\,\text{dB}$ [Fig. 10(a)]. This means that in the worst case, the mismatch between the actual object and the reconstructed one is around 0.1%. Moreover, it is worth noticing that the internal errors are of the order of 1% in severe noisy conditions (i.e., $SNR = \{5, 10\}$ dB) and decreases for higher SNRs. Furthermore, the background is free of artifacts with errors strictly below 0.1% [Fig. 10(a)].

Conversely, the noise impacts in a more significant way on the computational costs. As shown in Fig. 11, the number of interval evaluations to achieve the convergence grows with the noise level as well as the the number of admissible intervals at $k = K$ (i.e., it is more difficult to delete intervals in the presence of significant noise levels). Besides the growing difficulties when dealing with noisy environments as for standard state-of-the-art approaches, Table 5 indicates that the best intervals $[\underline{P}]^{opt}$ among the $I^{(K)}$ admissible at the convergence

are substantially the same for a wide range of SNR values (i.e., $SNR \geq 15\,\text{dB}$) further assessing the robustness and effectiveness of the IA-based strategy.

4.3. Performance Analysis against Dimensions and Contrasts

To assess the IA-inversion performance when modifying the parameters of the actual scatterer, the first experiment of this section considers the radius of the circular object, located at $(x_c^{act}, y_c^{act}) = (0.25\lambda, 0.125\lambda)$, varying between $\rho^{act} = 0.125\lambda$ up to $\rho^{act} = 0.5\lambda$. The IA-based optimization process has been run starting from the initial intervals $[\underline{P}]^{(0)}$ in Table 1. The final results are summarized in Fig. 12 where the values of the errors are plotted. As an indicative result, let us consider that the total error is always smaller than 1% whatever ρ.

For illustrative purposes, Fig. 13 reports both the actual scatterers [Fig. 13(a) and Fig. 13(c)] and the corresponding reconstructions [Fig. 13(b) and Fig. 13(d)] in correspondence with two representative

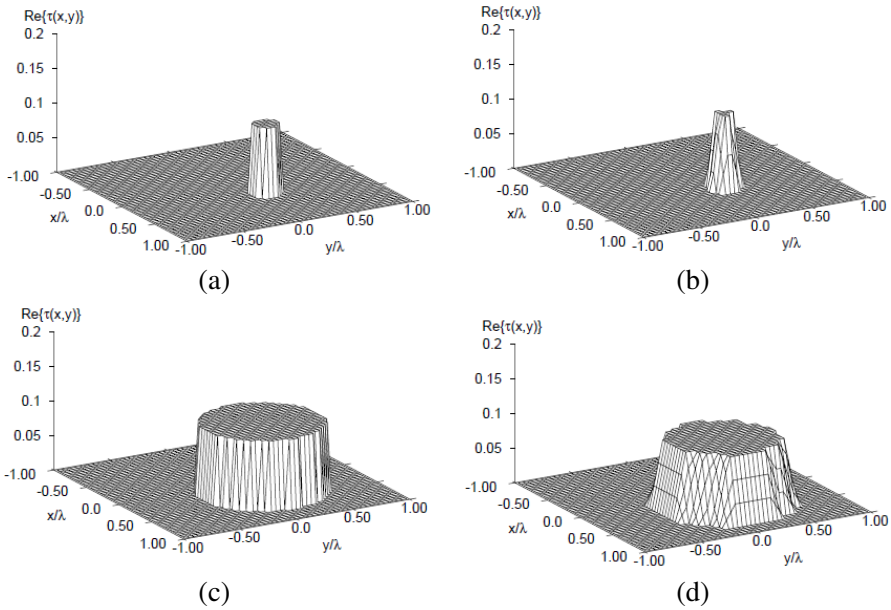

Figure 13. Off-centered homogeneous circular cylinder [$\rho = \{\frac{\lambda}{8}, \frac{\lambda}{2}\}$, $\tau = 0.1$, $(x_c, y_c) = (\frac{\lambda}{4}, \frac{\lambda}{8})$, $SNR = 50\,\text{dB}$]. Object Reconstruction — Distribution of the (a)(c) actual and (b)(d) reconstructed object function for (a)(b) $\rho = \frac{\lambda}{8}$ and (c)(d) $\rho = \frac{\lambda}{2}$.

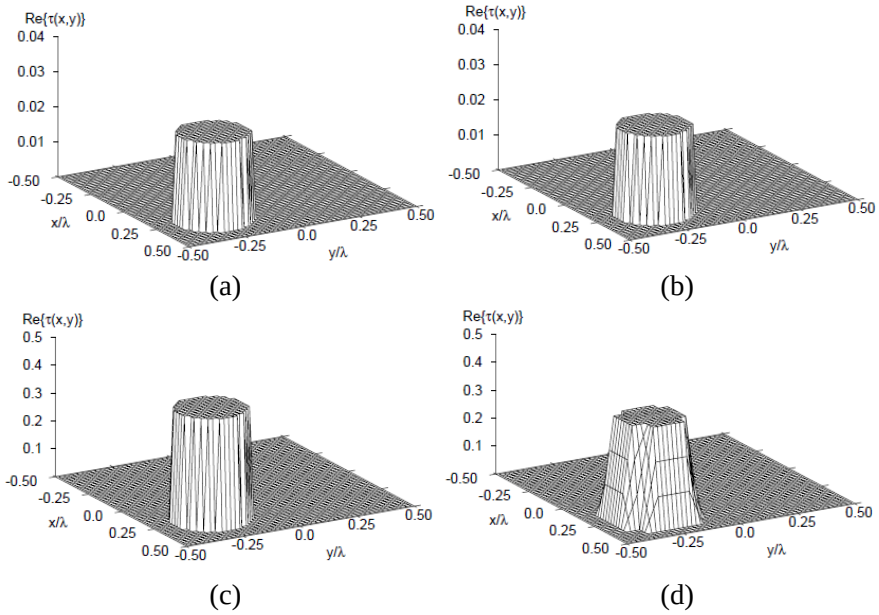

Figure 14. Off-centered homogeneous circular cylinder [$\rho = \frac{\lambda}{4}$, $\tau = \{0.025, 0.4\}$, $(x_c, y_c) = (\frac{\lambda}{4}, -\frac{\lambda}{4})$, $SNR = 50\,\text{dB}$]. Object Reconstruction — Distribution of the (a)(c) actual and (b)(d) reconstructed object function for (a)(b) $\tau = 0.025$ and (c)(d) $\tau = 0.4$.

test cases: $\rho^{act} = 0.125\lambda$ and $\rho^{act} = 0.5\lambda$. As it can be observed, the retrieved profiles are very close to the actual ones and the existing mismatch is mainly due to the different discretization used in the forward and the inversion problems.

In the second experiment, the performance of the IA-based method has been evaluated by changing the values of the permittivity as well as the dimension of the investigation domain, but still within the first-order Born approximation [63]. As an example, the size of Γ_{inv} has been reduced to $L = \lambda$ and the cylinder center and its radius have been fixed to $(x_c^{act}, y_c^{act}) = (0.25\lambda, -0.25\lambda)$ and $\rho = 0.25\lambda$, respectively, while the contrast has been varied between $\tau = 0.025$ and $\tau = 0.4$. By choosing the inversion grid of $N_{inv} = 20 \times 20$ cells and the initial values of the intervals as in Table 6, the final reconstructions for two representative contrasts (i.e., $\tau = 0.025$ and $\tau = 0.4$) are shown in Fig. 14. As expected and analogously to the previous tests, the IA inversions provide faithful reconstructions with reduced or sometimes negligible errors (Fig. 15).

Table 5. Off-centered homogeneous circular cylinder [$\rho = \frac{\lambda}{4}$, $\tau = 0.1$, $(x_c, y_c) = (-\frac{\lambda}{2}, -\frac{\lambda}{2})$, $SNR \in [5, 50]$ dB]. *Object Reconstruction* — Intervals containing the best solutions retrieved by means of the IA-based approach for different level of SNR.

SNR [dB]	$[x_c]$	$[y_c]$
5	$[-0.514649, -0.484375]$	$[-0.544922, -0.514648]$
10	$[-0.514649, -0.484375]$	$[-0.514649, -0.484375]$
15	$[-0.514649, -0.484375]$	$[-0.514649, -0.484375]$
20	$[-0.514649, -0.484375]$	$[-0.514649, -0.484375]$
25	$[-0.514649, -0.484375]$	$[-0.514649, -0.484375]$
30	$[-0.514649, -0.484375]$	$[-0.514649, -0.484375]$
50	$[-0.514649, -0.484375]$	$[-0.514649, -0.484375]$
SNR [dB]	$[\rho]$	$[\tau]$
5	$[0.212890, 0.243165]$	$[0.090981, 0.090983]$
10	$[0.212890, 0.243165]$	$[0.088838, 0.088843]$
15	$[0.212890, 0.243165]$	$[0.094070, 0.094080]$
20	$[0.212890, 0.243165]$	$[0.097128, 0.097138]$
25	$[0.212890, 0.243165]$	$[0.096807, 0.096827]$
30	$[0.212890, 0.243165]$	$[0.097357, 0.097376]$
50	$[0.212890, 0.243165]$	$[0.097576, 0.097596]$

Table 6. Off-centered homogeneous circular cylinder [$\rho = \frac{\lambda}{4}$, $\tau = \{0.025, 0.4\}$, $(x_c, y_c) = (\frac{\lambda}{4}, -\frac{\lambda}{4})$, $SNR = 50$ dB]. *Initialization* — Intervals considered at the initialization $k = 0$ of the IA-based optimization process.

Unknown Parameter Intervals	*Feasible Solution Space*
$[\tau]^{(0)} = \left[\left(\tau^L\right)_1^{(0)}, \left(\tau^R\right)_1^{(0)}\right]$	$[0.0, 0.4]$
$[\rho]^{(0)} = \left[\left(\rho^L\right)_1^{(0)}, \left(\rho^R\right)_1^{(0)}\right]$	$[0.025\lambda, 1.0\lambda]$
$[x_c]^{(0)} = \left[\left(x_c^L\right)_1^{(0)}, \left(x_c^R\right)_1^{(0)}\right]$	$\left[\left(-0.5 + \left(\rho^L\right)_1^{(0)}\right)\lambda, \left(0.5 - \left(\rho^L\right)_1^{(0)}\right)\lambda\right]$
$[y_c]^{(0)} = \left[\left(y_c^L\right)_1^{(0)}, \left(y_c^R\right)_1^{(0)}\right]$	$\left[\left(-0.5 + \left(\rho^L\right)_1^{(0)}\right)\lambda, \left(0.5 - \left(\rho^L\right)_1^{(0)}\right)\lambda\right]$

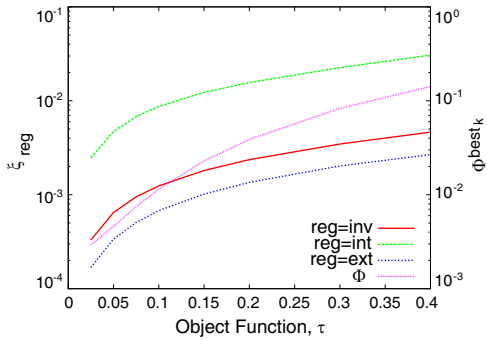

Figure 15. Off-centered homogeneous circular cylinder [$\rho = \frac{\lambda}{4}$, $\tau \in [0.025, 0.4]$, $(x_c, y_c) = (\frac{\lambda}{4}, -\frac{\lambda}{4})$, $SNR = 50\,\text{dB}$]. Error Indexes and Fitness Function - Values of the total, internal, and external error indexes and of the fitness function of the best solutions retrieved by means of the IA-based approach for different values of the object function: $\tau = \{0.025, 0.5, 0.75, 1.0, 1.5, 2.0, 3.0, 4.0\}$.

5. OUTCOMES AND CONCLUSIONS

The arithmetic of intervals and Interval Analysis have been applied for the first time, to the best of the authors' knowledge, to the solution of electromagnetic inverse scattering problems. The problem, reformulated according to the arithmetic of intervals, has been faced by means of an optimization strategy based on IA able to:

- find the global solution by eliminating, according to effective tests on the intervals processed at each iteration, the regions of the solution space not containing the minimum values of the cost functional at hand;
- consider the whole solution space not limiting the analysis to a portion of it;
- obtain the final solution in a finite number of iterations by exploiting stopping conditions naturally defined on the required accuracy of the expected solution.

The reported results have proved the effectiveness of the proposed approach in reconstructing weak scatterers when solving first-order Born approximation inversion problems. Moreover, its robustness to noisy data has been assessed.

As final remarks, it is worth pointing out that the IA-based method guarantees to reach the global optimum, while its main drawback lies in the computational burden that grows exponentially

with the number of unknowns making unfeasible pixel-based inversions and intractable high-dimensional problems. On the other hand, since there is a great attention towards model-based strategies, mainly to enable $3D$ imaging and/or the reconstruction of large $2D$ scenarios, it is authors' opinion that IA can play a key-role in such a framework especially when facing inverse scattering problems where the retrieval of the exact solution is mandatory and real-time performances are not necessary.

Future works, currently under development, but out-of-the-scope of this paper, are concerned with the extension of the range of applicability beyond Born approximation as well as to different parameterization. Of course, the computational issues are argument of a continuous evolution for overcoming current limitations of IA-based techniques as applied to inversion.

APPENDIX A. INTERVAL DEFINITION

Let us suppose $x \in \Re$ being a real variable. A closed real interval $[x] = [x^L, x^R]$ consists of the set of real numbers x such that $\{x: x^L \leq x \leq x^R\}$, where x^L and x^R are the left (minimum) and right (maximum) endpoints of the interval. Geometrically, $[x]$ can be represented by a segment on a line. As far as the value x is concerned, it is equivalent to the interval $[x, x]$, which is indicated as *degenerate* interval.

If the variable is complex, z, the closed interval $[z] = [z^L, z^R]$ stands for a two-dimensional box, namely a rectangular parallelepiped, whose sides are $a = |\Re\{z^R\} - \Re\{z^L\}|$ and $b = |\Im\{z^R\} - \Im\{z^L\}|$, $\Re\{\cdot\}$ and $\Im\{\cdot\}$ being the real and imaginary parts, respectively, and $|\cdot|$ the absolute value.

APPENDIX B. INTERVAL ARITHMETIC

Let us denote with "+", "−", "∗" and "/" the operators of addition, subtraction, multiplication and division, respectively. Let *op* be any of these operations for the arithmetic of the real numbers x and y, then the corresponding operation for the arithmetic of interval numbers $[x]$ and $[y]$ is

$$([x]\, op\, [y]) = \{x\, op\, y \,:\, x \in [x],\, y \in [y]\}\,. \tag{B1}$$

From (B1), it follows that the interval $([x]\, op\, [y])$ contains every possible value $x\, op\, y$ for each $x \in [x]$ and $y \in [y]$. Accordingly, the endpoints of $[x]\, op\, [y]$ are determined from the knowledge of the endpoints of $[x]$ and $[y]$. More specifically

(1) ***Interval Sum***
Let $[x] = [x^L, x^R]$ and $[y] = [y^L, y^R]$ be two real intervals. The sum operation is defined as

$$[x] + [y] = \left[x^L + y^L,\, x^R + y^R\right]; \tag{B2}$$

(2) ***Interval Subtraction***
Let $[x] = [x^L, x^R]$ and $[y] = [y^L, y^R]$ be two real intervals. The subtraction operation is defined as

$$[x] - [y] = \left[x^L - y^R,\, x^R - y^L\right]; \tag{B3}$$

(3) ***Interval Multiplication***
Let $[x] = [x^L, x^R]$ and $[y] = [y^L, y^R]$ be two real intervals. The multiplication operation is defined as

$$\begin{aligned}[x] * [y] \;=\; &\left[\min\left(x^L y^L,\, x^L y^R,\, x^R y^L,\, x^R y^R\right),\right.\\ &\left.\max\left(x^L y^L,\, x^L y^R,\, x^R y^L,\, x^R y^R\right)\right];\end{aligned} \tag{B4}$$

(4) ***Interval Inverse***
Let $[y] = \left[y^L, y^R\right]$ be a real interval. The inverse interval $1/[y]$ is defined as

$$\frac{1}{[y]} = \left[\frac{1}{y^R},\, \frac{1}{y^L}\right] \quad 0 \notin [y]; \tag{B5}$$

(5) ***Interval Division***
Let $[x] = [x^L, x^R]$ and $[y] = \left[y^L, y^R\right]$ be two real intervals. The interval division is defined by means of the interval inverse and the interval multiplication as

$$\frac{[x]}{[y]} = [x] * \left(\frac{1}{[y]}\right) \quad 0 \notin [y]; \tag{B6}$$

(6) ***Interval Power***
Let $[x] = [x^L, x^R]$ be a real interval. The power operation is defined as

$$[x]^n = \begin{cases} [1,\, 1] & \text{if (n=0)} \\ \left[\left(x^L\right)^n, \left(x^R\right)^n\right] & \text{if } \left(x^L \geq 0\right) \text{ or } \left[\left(x^L \leq 0 \leq x^R\right)\right. \\ & \left.\text{and } (n \text{ is odd})\right] \\ \left[\left(x^R\right)^n, \left(x^L\right)^n\right] & \text{if } \left(x^R \leq 0\right) \\ \left[0, \max\left\{\left(x^L\right)^n, \left(x^R\right)^n\right\}\right] & \text{if } \left[\left(x^L \leq 0 \leq x^R\right)\right. \\ & \left.\text{and } (n \,\text{is, even})\right] \end{cases}; \tag{B7}$$

APPENDIX C. FUNDAMENTAL THEOREM OF IA

Let us consider a real-valued function f of N real variables $x_1, \ldots, x_N$ and an interval function $[f]$ of interval variables $[x]_1, \ldots, [x]_N$. The interval function $[f]$ is an *interval extension* of f if

$$[f(x_1, \ldots, x_N)] = f(x_1, \ldots, x_N) \tag{C1}$$

for all $x_n,\ n = 1, \ldots, N$. This means that if the arguments of $[f]$ are degenerate intervals then $[f([x]_1, \ldots, [x]_N)]$ is a degenerate interval function equal to $f(x_1, \ldots, x_N)$.

In case $[x]_n \subset [y]_n,\ n = 1, \ldots, N$ and the following condition holds true

$$[f([x]_1, \ldots, [x]_N)] \subset [f([y]_1, \ldots, [y]_N)]. \tag{C2}$$

$[f]$ is said to be *inclusion monotonic*. By virtue of (B1), it is possible to state that the arithmetic of intervals is inclusion monotonic and therefore if $[x]_n \subset [y]_n,\ n = 1, 2$ then

$$([x]_1 \, op \, [x]_2) \subset ([y]_1 \, op \, [y]_2)\,. \tag{C3}$$

The *Fundamental Theorem of Interval Analysis* [68] states that being $[f([x]_1, \ldots, [x]_N)]$ an inclusion monotonic interval extension of a real function $f(x_1, \ldots, x_N)$, then $[f([x]_1, \ldots, [x]_N)]$ contains the whole values of $f(x_1, \ldots, x_N)$ for all $x_n \in [x]_N,\ n = 1, \ldots, N$.

The main outcomes from the *Fundamental Theorem of Interval Analysis* are that:

- If a real function f is evaluated on an interval by means of an inclusion monotonic extension F, the resulting interval contains all the values of f within the interval;
- There is no unique interval extension $[f]$ of a given function f;
- The best interval extension of a given function is that where $[f([x]_1, \ldots, [x]_N)] = \{f(x_1, \ldots, x_N)\colon\ x_n \in [x]_n,\ n = 1, \ldots, N\}$, $[f([x]_1, \ldots, [x]_N)]$ being an inclusion monotonic interval extension of a real function $f(x_1, \ldots, x_N)$. It means that the resulting interval function $[f]$ contains exactly the range of f over the set of values $x_n \in [x]_n,\ n = 1, \ldots, N$;
- The best interval extension of f can be computed only if f can be expressed in a form where every independent interval is considered only once.

REFERENCES

1. Bertero, M. and P. Boccacci, *Introduction to Inverse Problems in Imaging*, IOP Press, Bristol, U.K., 1998.

2. Massa, A. and S. Caorsi, *Special Issue on 'Microwave Imaging and Inverse Scattering Techniques'*, Vol. 16, No. 2, 2003, ISSN 0920-5071.
3. Lesselier, D. and T. Habashy, "Special issue on 'Electromagnetic imaging and inversion on the Earth's subsurface'," *Inverse Probl.*, Vol. 16, No. 5, 2000.
4. Chew, W. C. and D. Lesseliser, "Special issue on 'Electromagnetic characterization of buried obstacles'," *Inverse Probl.*, Vol. 20, No. 6, 2004.
5. Zhang, X., H. Tortel, S. Ruy, and A. Litman, "Microwave imaging of soil water diffusion using the linear sampling method," *IEEE Geosci. Remote Sens. Lett.*, Vol. 8, No. 3, 421–425, 2011.
6. Caorsi, S., A. Massa, and M. Pastorino, "A crack identification microwave procedure based on a genetic algorithm for nondestructive testing," *IEEE Trans. Antennas Propag.*, Vol. 49, No. 12, 1812–1820, 2001.
7. Benedetti, M., M. Donelli, and A. Massa, "Multicrack detection in two-dimensional structures by means of GA-based strategies," *IEEE Trans. Antennas Propag.*, Vol. 55, No. 1, 205–215, 2007.
8. Mudanyal, O., S. Yldz, O. Semerci, A. Yapar, and I. Akduman, "A microwave tomographic approach for nondestructive testing of dielectric coated metallic surfaces," *IEEE Geosci. Remote Sens. Lett.*, Vol. 5, No. 2, 180–184, 2008.
9. Ma, Y.-K., P.-S. Kin, and W.-K. Park, "Analysis of topological derivative function for a fast electromagnetic imaging of perfectly conducing cracks," *Progress In Electromagnetics Research*, Vol. 122, 311–325, 2012.
10. Joh, Y.-D. and W.-K. Park, "Structural behavior of the Music-type algorithm for imaging perfectly conducting cracks," *Progress In Electromagnetics Research*, Vol. 138, 211–226, 2013.
11. Bindu, G. N., S. J. Abraham, A. Lonappan, V. Thomas, C. K. Aanandan, and K. T. Mathew, "Active microwave imaging for breast cancer detection," *Progress In Electromagnetics Research*, Vol. 58, 149–169, 2006.
12. Zhang, H., S. Y. Tan, and H. S. Tan, "A novel method for microwave breast cancer detection," *Progress In Electromagnetics Research*, Vol. 83, 413–434, 2008.
13. Zhou, H., T. Takenaka, J. E. Johnson, and T. Tanaka, "Breast imaging model using microwaves and a time domain three dimensional reconstruction method," *Progress In Electromagnetics Research*, Vol. 93, 57–70, 2009.

14. Henriksson, T., N. Joachimowicz, C. Conessa, and J.-C. Bolomey, "Quantitative microwave imaging for breast cancer detection using a planar 2.45 GHz system," *IEEE Trans. Instrum. Meas.*, Vol. 59, No. 10, 2691–2699, 2010.
15. Ashtari, A., S. Noghanian, A. Sabouni, J. Aronsson, G. Thomas, and S. Pistorius, "Using a priori information for regularization in breast microwave image reconstruction," *IEEE Trans. Biomed. Eng.*, Vol. 57, No. 9, 2197–2208, 2010.
16. Bozza, G., M. Brignone, and M. Pastorino, "Application of the no-sampling linear sampling method to breast cancer detection," *IEEE Trans. Biomed. Eng.*, Vol. 57, No. 10, 2525–2534, 2010.
17. Flores-Tapia, D., M. O'Halloran, and S. Pistorius, "A bimodal reconstruction method for breast cancer imaging," *Progress In Electromagnetics Research*, Vol. 118, 461–486, 2011.
18. Hagness, S., E. Fear, and A. Massa, "Special cluster on "Microwave medical imaging," *IEEE Antennas Wireless Propagat. Lett.*, Vol. 11, 1592–1597, 2012.
19. Davy, M., T. Lepetit, J. de Rosny, C. Prada, and M. Fink, "Detection and imaging of human beings behind a wall using the Dort method," *Progress In Electromagnetics Research*, Vol. 110, 353–369, 2010.
20. Zhang, W., A. Hoorfar, and L. Li, "Through-the-wall target localization with time reversal Music method," *Progress In Electromagnetics Research*, Vol. 106, 75–89, 2010.
21. Lu, T., K. Agarwal, Y. Zhong, and X. Chen, "Through-wall imaging: Application of subspace-based optimization method," *Progress In Electromagnetics Research*, Vol. 102, 351–366, 2010.
22. Catapano, I. and L. Crocco, "A qualitative inverse scattering method for through-the-wall imaging," *IEEE Geosci. Remote Sens. Lett.*, Vol. 7, No. 4, 685–689, 2010.
23. Burkholder, R. J. and K. E. Browne, "Coherence factor enhancement of through-wall radar images," *IEEE Antennas Wireless Propag. Lett.*, Vol. 9, 842–845, 2010.
24. Soldovieri, F., F. Ahmad, and R. Solimene, "Validation of microwave tomographic inverse scattering approach via through-the-wall experiments in semicontrolled conditions," *IEEE Geosci. Remote Sens. Lett.*, Vol. 8, No. 1, 123–127, 2011.
25. Dorn, O. and D. Lesselier, "Special issue on 'Electromagnetic inverse problems: Emerging methods and novel applications'," *Inverse Probl.*, Vol. 26, No. 7, 2010.

26. Bucci, O. M. and G. Franceschetti, "On the degrees of freedom of scattered fields," *IEEE Trans. Antennas Propag.*, Vol. 37, No. 7, 918–926, 1989.
27. Bucci, O. M. and T. Isernia, "Electromagnetic inverse scattering: Retrievable information and measurement strategies," *Radio Sci.*, Vol. 32, No. 6, 2123–2137, 1997.
28. Isernia, T., V. Pascazio, and R. Pierri, "On the local minima in a tomographic imaging technique," *IEEE Trans. Geosci. Remote Sens.*, Vol. 39, No. 7, 1596–1607, 2001.
29. D'Urso, M., T. Isernia, and A. F. Morabito, "On the solution of 2-D inverse scattering problems via source-type integral equations," *IEEE Trans. Geosci. Remote Sens.*, Vol. 48, No. 3, 1186–1198, 2010.
30. Agarwal, K., L. Pan, and X. Chen, "Subspace-based optimization method for reconstruction of 2-D complex anisotropic dielectric objects," *IEEE Trans. Microw. Theory Tech.*, Vol. 58, No. 4, 1065–1074, 2010.
31. Estatico, C., G. Bozza, A. Massa, M. Pastorino, and A. Randazzo, "A two steps inexact-Newton method for electromagnetic imaging of dielectric structures from real data," *Inverse Probl.*, Vol. 21, No. 6, 81–94, 2005.
32. Barriere, P., J. Idier, Y. Goussard, and J. Laurin, "Fast solutions of the 2D inverse scattering problem based on a TSVD approximation of the internal field for the forward model," *IEEE Trans. Antennas Propag.*, Vol. 58, 4015–4024, 2010.
33. Li, J., X. Wang, and T. Wang, "On the validity of Born approximation," *Progress In Electromagnetics Research*, Vol. 107, 219–237, 2010.
34. Poli, L., G. Oliveri, and A. Massa, "Microwave imaging within the first-order Born approximation by means of the contrast-field Bayesian compressive sensing," *IEEE Trans. Antennas Propagat.*, Vol. 60, 2865–2879, 2012.
35. Oliveri, G., L. Poli, P. Rocca, and A. Massa, "Bayesian compressive optical imaging within the Rytov approximation," *Opt. Lett.*, Vol. 37, 1760–1762, 2012.
36. Winters, D. W., B. D. Van Veen, and S. C. Hagness, "A sparsity regularization approach to the electromagnetic inverse scattering problem," *IEEE Trans. Antennas Propag.*, Vol. 58, No. 1, 145–154, 2010.
37. Oliveri, G., P. Rocca, and A. Massa, "A Bayesian-compressive-sampling-based inversion for imaging sparse scatterers," *IEEE*

Trans. Geosci. Remote Sens., Vol. 49, No. 10, 3993–4006, 2011.

38. Poli, L., G. Oliveri, P. Rocca, and A. Massa, "Bayesian compressive sensing approaches for the reconstruction of two-dimensional sparse scatterers under TE illuminations," *IEEE Trans. Geosci. Remote Sens.*, Vol. 51, 2920–2936, 2013.
39. Viani, F., L. Poli, G. Oliveri, F. Robol, and A. Massa, "Sparse scatterers imaging through approximated multi-task compressive sensing strategies," *Microwave Opt. Technol. Lett.*, Vol. 55, 1553–1557, 2013.
40. Rekanos, I. T., "Neural-network-based inverse-scattering technique for online microwave medical imaging," *IEEE Trans. Mag.*, Vol. 38, No. 2, 1061–1064, 2002.
41. Massa, A., A. Boni, and M. Donelli, "A classification approach based on SVM for electromagnetic subsurface sensing," *IEEE Trans. Geosci. Remote Sens.*, Vol. 43, No. 9, 2084–2093, 2005.
42. Bermani, E., A. Boni, A. Kerhet, and A. Massa, "Kernels evaluation of SVM-based estimators for inverse scattering problems," *Progress In Electromagnetics Research*, Vol. 53, 167–188, 2005.
43. Miller, E. L. and A. S. Willsky, "A multiscale, statistically based inversion scheme for linearized inverse scattering problems," *IEEE Trans. Geosci. Remote Sens.*, Vol. 34, No. 2, 346–357, 1996.
44. Caorsi, S., M. Donelli, and A. Massa, "Detection, location and imaging of multiple scatterers by means of the iterative multiscaling method," *IEEE Trans. Microw. Theory Tech.*, Vol. 52, No. 4, 1217–1228, 2004.
45. Poli, L. and P. Rocca, "Exploitation of TE-TM scattering data for microwave imaging through the multi-scaling reconstruction strategy," *Progress In Electromagnetics Research*, Vol. 99, 245–260, 2009.
46. Rocca, P., M. Donelli, G. L. Gragnani, and A. Massa, "Iterative multi- resolution retrieval of non-measurable equivalent currents for imaging purposes," *Inverse Probl.*, Vol. 25, No. 5, 1–25, 2009.
47. Rocca, P., "Multi-resolution retrieval of non-measurable equivalent currents in microwave imaging problems — Experimental assessment," *Progress In Electromagnetics Research*, Vol. 96, 267–285, 2009.
48. Lee, Y.-S., C.-C. Chiu, and Y.-S. Lin, "Electromagnetic imaging for an imperfectly conducting cylinder buried in a three-layer structure by the genetic algorithm," *Progress In Electromagnetics Research*, Vol. 48, 27–44, 2004.

49. Chen, X., K.-M. Huang, and X.-B. Xu, "Microwave imaging of buried inhomogeneous objects using parallel genetic algorithm combined with FDTD method," *Progress In Electromagnetics Research*, Vol. 53, 283–298, 2005.
50. Semnani, A. and M. Kamyab, "An enhanced method for inverse scattering problems using Fourier series expansion in conjunction with FDTD and PSO," *Progress In Electromagnetics Research*, Vol. 76, 45–64, 2007.
51. Huang, C.-H., C.-C. Chiu, C.-L. Li, and K.-C. Chen, "Time domain inverse scattering of a two-dimensional homogenous dielectric object with arbitrary shape by particle swarm optimization," *Progress In Electromagnetics Research*, Vol. 82, 381–400, 2008.
52. Semnani, A. and M. Kamyab, "Truncated cosine Fourier series expansion method for solving 2-D inverse scattering problems," *Progress In Electromagnetics Research*, Vol. 81, 73–97, 2008.
53. Brignone, M., G. Bozza, A. Randazzo, M. Piana, and M. Pastorino, "A hybrid approach to 3D microwave imaging by using linear sampling and ACO," *IEEE Trans. Antennas Propag.*, Vol. 56, No. 10, 3224–3224, 2008.
54. Rocca, P., M. Benedetti, M. Donelli, D. Franceschini, and A. Massa, "Evolutionary optimization as applied to inverse scattering problems," *Inverse Probl.*, Vol. 25, 123003, 1–41, 2009.
55. Semnani, A., I. T. Rekanos, M. Kamyab, and T. G. Papadopoulos, "Two-dimensional microwave imaging based on hybrid scatterer representation and differential evolution," *IEEE Trans. Antennas Propag.*, Vol. 58, No. 10, 3289–3298, 2010.
56. Moore, R., *Interval Analysis*, Prentice-Hall, Englewood Cliffs, New Jersey, USA, 1966.
57. Hansen, E., "On solving systems of equations using interval arithmetic," *Mathematics of Computation*, Vol. 22, No. 102, 374–384, 1968.
58. Neumaier, A., "Interval iteration for zeros of systems of equations," *BIT*, Vol. 25, No. 1, 256–273, 1985.
59. Saxena, G. and D. A. Lowther, "The use of interval mathematics in electromagnetic design," *IEEE Trans. Mag.*, Vol. 37, No. 5, 3588–3591, 2001.
60. Egiziano, L., P. Lamberti, G. Spagnuolo, and V. Tucci, "Robust design of electromagnetic systems based on interval Taylor extension applied to a multiquadric performance function," *IEEE Trans. Mag.*, Vol. 44, No. 6, 1134–1137, 2008.

61. Soares, G. L., A. Arnold-Bos, L. Jaulin, C. A. Maia, and J. A. Vasconcelos, "An interval-based target tracking approach for range-only multistatic radar," *IEEE Trans. Mag.*, Vol. 44, No. 6, 1350–1353, 2008.
62. Chew, W. C., *Waves and Fields in Inhomogeneous Media*, IEEE Press, New York, 1995.
63. Slaney, M., A. C. Kak, and L. E. Larsen, "Limitations of imaging with first-order diffraction tomography," *IEEE Trans. Microw. Theory Tech.*, Vol. 32, No. 8, 860–874, 1984.
64. Caorsi, S. and M. Pastorino, "Two-dimensional microwave imaging approach based on a genetic algorithm," *IEEE Trans. Antennas Propag.*, Vol. 48, No. 3, 370–373, 2000.
65. Richmond, J. H., "Scattering by a dielectric cylinder of arbitrary cross section shape," *IEEE Trans. Antennas Propag.*, Vol. 13, No. 3, 334–341, 1965.
66. Colton, D. and R. Kress, *Inverse Acoustic and Electromagnetic Scattering Theory*, Springer-Verlag, Berlin, Germany, 1992.
67. Hansen, E., "Global optimization using interval analysis — The multi-dimensional case," *Numer. Math.*, Vol. 34, 247–270, 1980.
68. Rall, L. B., *Computational Solution of Nonlinear Operator Equations*, Wiley, New York, 1969.
69. Caorsi, S., M. Donelli, and A. Massa, "Analysis of the stability and robustness of the iterative multi-scaling approach for microwave imaging applications," *Radio Sci.*, Vol. 39, 1–17, 2004.